Journal of Zhejiang University-SCIENCE A (Applied Physics & Engineering) 2023 24(8):710-721
www.jzus.zju.edu.cn; www.springer.com/journal/11582
E-mail: jzus_a@zju.edu.cn

Research Article

https://doi.org/10.1631/jzus.A2200490

Co_3O_4-ZnO/rGO catalyst preparation and rhodamine B degradation by sulfate radical photocatalysis

Zhanmei ZHANG[1,2]✉, Yi ZHANG[1], Xilin CHEN[1], Ziran HUANG[1], Zuqin ZOU[1], Huaili ZHENG[3]

[1]*Key Laboratory of Hydraulic and Waterway Engineering of the Ministry of Education, School of River and Ocean Engineering, Chongqing Jiaotong University, Chongqing 400074, China*
[2]*National Engineering Research Center for Inland Waterway Regulation, Chongqing 400074, China*
[3]*College of Environment and Ecology, Chongqing University, Chongqing 400044, China*

Abstract: The development of a combined photocatalytic system with peroxymonosulfate (PMS) has great potential applications in the degradation and treatment of aqueous organic pollutants. Herein, a Co_3O_4-ZnO/rGO was prepared by a hydrothermal method using cobalt acetate, zinc acetate, and reduced graphene oxide (rGO) as the main raw materials. The physical and chemical characteristics of the obtained catalyst were analyzed using X-ray diffraction (XRD), X-ray photoelectron spectroscopy (XPS), scanning electron microscopy (SEM), and Fourier transform infrared (FT-IR). The photocatalytic features and capacities of the catalytic materials to activate PMS were investigated. Co_3O_4-ZnO/rGO exhibited stronger photocatalytic activity and ability to activate PMS than Co_3O_4/rGO or ZnO/rGO, and significantly improved the ability of PMS and photocatalysis to synergistically degrade rhodamine B (RhB), with a degradation rate of 90.40% within 40 min. The mechanism of RhB degradation was proposed based on characterization of materials, evaluation of RhB degradation efficiency, and analysis of the active species involved. The unique particle/sheet structure of Co_3O_4-ZnO/rGO provides a large number of active sites, and the formation of heterojunctions between Co_3O_4 and ZnO improves carrier separation and transport in the reaction system. Our study offers a reference for designing more effective heterojunction catalysts based on the combination of PMS and photocatalytic technology.

Key words: Co_3O_4-ZnO/rGO catalyst; Rhodamine B (RhB); Heterojunction; Photocatalysis; Peroxymonosulfate (PMS)

1 Introduction

Over the past decade, the gradual intensification of water pollution has become a major concern (Yang ZH et al., 2019). Rhodamine B (RhB) is used extensively as a synthetic basic dye in numerous applications in the textile, leather, and plastic industries. However, RhB is chemically stable, tends to accumulate in the environment, is highly toxic and carcinogenic, and causes harm to humans and aquatic organisms even at low concentrations in wastewater. Advanced oxidation processes utilize strongly oxidizing reactive free radicals to effectively degrade various pollutants and are widely used in environmental treatments because of their high oxidation efficiency and fast degradation rate (Ghanbari and Moradi, 2017; Cao et al., 2020). Compared with traditional technologies, photocatalytic technology has attracted increasing attention because of its environmental remediation potential and low cost (Gautam et al., 2020; Malefane et al., 2020). However, because they are limited by the narrow absorption range of ultraviolet (UV) light, the catalysts have low light-energy utilization efficiency in practical applications, which affects their photocatalytic degradation potential. Moreover, photocatalytic systems alone are not ideal for the treatment of polluted water bodies with low transmittance and high turbidity. In recent years, water pollution remediation has been greatly aided by the application of sulfate-radical-mediated photocatalysis (SR-photo) technology, which relies on the synergistic effects of photocatalysis and activated peroxymonosulfate (PMS) (Ren et al., 2018; Guo et al., 2020; Han et al., 2020). Under the influence of light and the catalyst in the SR-photo system, PMS can also produce other active species, such as sulfate ($SO_4^{\bullet-}$)

✉ Zhanmei ZHANG, zhanmei2003@126.com
Zhanmei ZHANG, https://orcid.org/0000-0001-7259-8011

Received Oct. 19, 2022; Revision accepted Feb. 10, 2023;
Crosschecked June 16, 2023

and hydroxyl radicals (·OH). Additionally, it can increase the effectiveness of photocatalytic oxidation reaction and decrease recombination of electron-hole pairs during the photocatalytic process (Zhang JL et al., 2020, 2021). However, this technique relies on the performance of the selected catalysts in terms of both their photocatalytic and PMS-activation properties. Therefore, finding a reliable and effective photocatalyst to activate PMS is crucial for the water-treatment industry.

Co_3O_4 is a p-type semiconductor with a narrow band gap (1.2–2.1 eV) and is widely used in photocatalysis because of its excellent stability and powerful light-absorption properties (Tang et al., 2016; Ren et al., 2020). In addition, studies have shown that Co (II) has a good activation effect on the PMS system (Yang J et al., 2019; Shen et al., 2020). However, as research on the photocatalytic efficacy of Co_3O_4 has expanded in recent years, photogenerated electrons of pure Co_3O_4 have been found to bind easily, which reduces its photocatalytic capacity (Guo et al., 2021). Moreover, the low Co_3O_4 redox potential (2.44 eV) renders the use of large quantities of Co_3O_4 as a photocatalyst difficult with regard to environmental purification (Tang et al., 2016). Numerous studies have shown that p-n heterojunctions formed by combining p- and n-type semiconductors can significantly reduce the compounding of photogenerated electron-hole pairs and enhance photocatalytic activity (Reda et al., 2017; Guo et al., 2018). ZnO is regarded as a suitable photocatalytic material and as an n-type semiconductor because of its nontoxicity, relatively low cost, and strong photochemical reactivity. At the p-n junction interface, the presence of p-type Co_3O_4 and n-type ZnO creates an advantageous internal electric field for photocatalysis, which may significantly decrease recombination of photogenerated electrons and holes and increase the efficiency of photoreactions (Dong et al., 2015).

Reduced graphene oxide (rGO) is an excellent semiconductor with a large pore size, specific surface area, and high electrical conductivity. It is widely used in the adsorption and oxidation of organic pollutants in wastewater and is widely studied as a carbon-based carrier (Li and Dong, 2019; Thakur and Kandasubramanian, 2019). Overall, the introduction of rGO into photocatalysts can significantly improve the photocatalytic activity of materials to enhance the efficient degradation of organic pollutants (Akbarzadeh et al., 2020). To our knowledge, no reports exist regarding the use of rGO-loaded Co_3O_4-ZnO heterojunction as a dual-effect catalyst to promote the degradation of RhB by a synergistic system of PMS and photocatalytic oxidation.

In this study, we investigated the capacity of a Co_3O_4-ZnO/rGO heterojunction catalyst produced by a hydrothermal method to degrade RhB in solution by activating PMS under UV light. In addition, the effects of different preparation conditions, such as the rGO doping amount, hydrothermal reaction time, and calcination temperature, on the catalyst performance were investigated. The primary active compounds generated throughout the degradation process and the synergistic effect of the UV/Co_3O_4-ZnO/rGO/PMS system on the RhB removal mechanism were investigated. This provides a feasible strategy for constructing efficient and reusable dual-effect heterojunction catalysts.

2 Materials and methods

2.1 Chemicals

rGO was supplied by The Sixth Element (Changzhou) Materials Technology Co. Ltd. (Changzhou, China). Potassium PMS was obtained from the Chengdu Kelong Chemical Reagent Factory (Chengdu, China). Other analytical grade reagents including sulfuric acid (H_2SO_4), sodium nitrate ($NaNO_3$), potassium permanganate ($KMnO_4$), hydrochloric acid (HCl), cobalt acetate ($Co(C_2H_3O_2)_2$), zinc acetate ($Zn(C_2H_3O_2)_2$), anhydrous ethanol, ammonia (NH_3-H_2O), tert-butanol (TBA), triethanolamine (TEOA), methanol (MeOH), and benzoquinone (BQ) were purchased from Chongqing Chuandong Chemical Co., Ltd. (Chongqing, China). RhB was purchased from Tianjin Guangfu Chemical Co. Ltd. (Tianjin, China).

2.2 Synthesis

We used a hydrothermal approach to generate the Co_3O_4-ZnO/rGO employed in the tests, and the precise processes are illustrated in Fig. 1.

First, 5-g rGO was dispersed in 15-mL deionized water, and the suspension was sonicated for 30 min. Cobalt acetate (0.2982 g) was weighed and added to 15-mL deionized water, stirred for 15 min to dissolve completely, and then mixed with the rGO suspension, after which 20-mL NH_3-H_2O was added to the mixed solution and stirred for 30 min. The mixed solution was condensed and refluxed in an oil bath at 100 °C for 4 h, and the bottle was opened to volatilize

NH_3-H_2O and then labeled as sample #1. Then, 0.505-g $Zn(CH_3COO)_2$ was dissolved in 20-mL deionized water, 5-mL NH_3-H_2O was added, and the mixture was condensed and refluxed for 2 h and labeled as sample #2. Afterward, samples #1 and #2 were mixed well, transferred into an autoclave, and reacted at 180 ℃ for 20 h. The suspension was then separated by centrifugation at 3000 r/min for 5 min, washed three times with deionized water and anhydrous ethanol, and dried at 60 ℃ for 8 h. Next, the powder was calcined at 500 ℃ for 2 h in a nitrogen-filled tube muffle furnace to obtain Co_3O_4-ZnO/rGO as the final product.

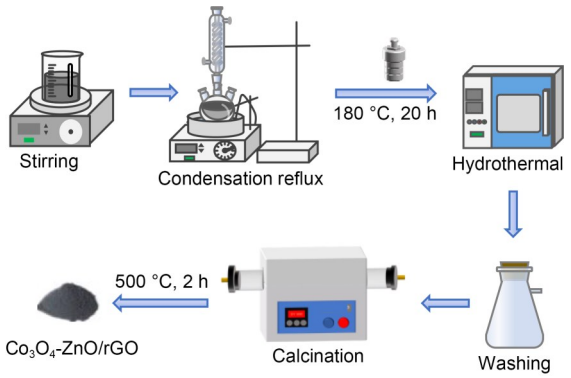

Fig. 1 Synthesis path of Co_3O_4-ZnO/rGO

2.3 Characterization

X-ray photoelectron spectroscopy (XPS) studies of surface chemical morphology were performed using a K-Alpha photoelectron spectrometer (Thermo Fisher Scientific, USA) with monochromatic Al Kα radiation at 15 kV. We obtained Fourier transform infrared (FT-IR) spectra using a Nicolet 670 spectrometer (Nicolet, USA) and analyzed the functional groups and chemical bonds of the materials using KBr as a reference in the spectral range of 4000–500 cm^{-1}. X-ray diffraction (XRD) curves were obtained using an X'Pert PRO instrument (PANAlytical, the Netherlands) with Cu Kα radiation with a 2θ range of 0°–90° and a sweep of 10°–90° at a rate of 5°/min. Sample morphology was examined by scanning electron microscopy (SEM) (ZEISS Gemini 300, Oberkochen, Germany), and the optical properties were determined by ultraviolet-visible diffuse reflectance spectrometry (UV-Vis DRS) (UV-3600, Shimadzu, Japan).

2.4 Experimental procedure

First, we examined the performance of the catalyst in relation to the rGO doping amount, duration of the hydrothermal reaction, and calcination temperature. Co_3O_4-ZnO/rGO with different rGO doping fractions (0.1%, 0.3%, 0.5%, 0.7%, and 0.9%) was added to 50-mg/L RhB, after which the catalytic performance was evaluated in terms of the RhB degradation rate. Similarly, we tested the catalytic performance of Co_3O_4-ZnO/rGO prepared at hydrothermal times of 3.0, 3.5, 4.0, 4.5, and 5.0 h and calcination temperatures of 300, 400, 500, 600, and 700 ℃.

The following three reaction systems were built: UV/Co_3O_4-ZnO/rGO/PMS, UV/Co_3O_4-ZnO/rGO, and Co_3O_4-ZnO/rGO/PMS. Beakers #1, #2, and #3 each contained 200-mL RhB solution (50 mg/L). Then, 0.125-g Co_3O_4-ZnO/rGO was added, and the mixture was magnetically stirred for 45 min under dark conditions. After that, 0.025-g PMS was added to beakers #1 and #2; beakers #1 and #3 were irradiated with UV, while beaker #2 remained in the dark, and reactions were allowed to continue in the three beakers for 1 h. Samples were collected regularly. Immediately after sampling, 1-mL MeOH was added to stop the reaction. The samples were centrifuged at 3000 r/min for 5 min, the supernatant was quickly collected, and a UV spectrophotometer was used to detect RhB absorbance at 554 nm, which was then converted into RhB concentration.

Furthermore, we investigated the stability and reusability of Co_3O_4-ZnO/rGO. After each experiment, the remaining catalyst was collected by centrifugation and washed three times with deionized water and ethanol and then dried at 60 ℃ for 8 h. While keeping the reaction conditions consistent, the experiment was repeated five times. The reusability of the material was determined based on its RhB degradation rate. The catalysts were characterized by XPS before and after the experiments, and the stability of the materials was determined by changes in the Co, Zn, and GO peak positions and corresponding intensities.

3 Results and discussion

3.1 Characterization

3.1.1 XRD

The XRD pattern in Fig. 2 reveals that the peak of Co_3O_4-ZnO/rGO had two components, Co_3O_4 (JCPDS, No. 43-1003) and ZnO (JCPDS, No. 36-1451) (Han et al., 2014; Lou et al., 2018). Peaks were observed at

19.3°, 34.4°, 44.7°, 54.9°, and 63.2° for 2θ, corresponding to the reflections of (111), (311), (400), (422), and (440), respectively. These corresponded well with the characteristic peaks of Co_3O_4 (Jin et al., 2020b). Similarly, the peaks corresponding to the characteristic peaks of ZnO were at 31.6°, 36.4°, 56.4°, 61.3°, and 67.7° for 2θ, corresponding to the (002), (102), (110), (103), and (220) reflections, respectively. Other characteristic peaks were also observed in the spectrum of Co_3O_4-ZnO/rGO, indicating the presence of impurities in the synthesized product. The peaks of Co_3O_4 and ZnO in Co_3O_4-ZnO/rGO produced a certain angle shift, which may have been caused by Co or Zn ions entering each other's lattices (Alshaikh et al., 2021).

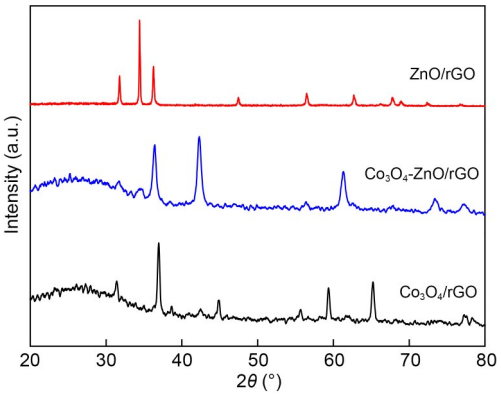

Fig. 2 XRD patterns of ZnO/rGO, Co_3O_4-ZnO/rGO, and Co_3O_4/rGO

3.1.2 FT-IR

Fig. 3 shows the FT-IR spectra of the three prepared materials. Two peaks can be observed at 572 and 667.5 cm^{-1} for Co_3O_4/rGO, corresponding to the vibrations of Co (II)–O and Co (III)–O, respectively. In the spectrum of ZnO/rGO, the peak at 483 cm^{-1} corresponds to the stretching vibration of Zn (II)–O (El-Molla et al., 2017; Yang J et al., 2019). All the characteristic peaks of the above two components are observable in the Co_3O_4-ZnO/rGO spectrum. In addition, the peak at 1634 cm^{-1} corresponds to the stretching vibration of the C═C SP^2 hybrid carbon atoms in reduced graphene oxide. The vibration of the water molecule–OH adsorbed on the catalyst surface was responsible for the absorption peak at 3419.5 cm^{-1} (Rakibuddin and Ananthakrishnan, 2016). Combined with the XRD characterization, the results showed that the material contained Co–O and Zn–O.

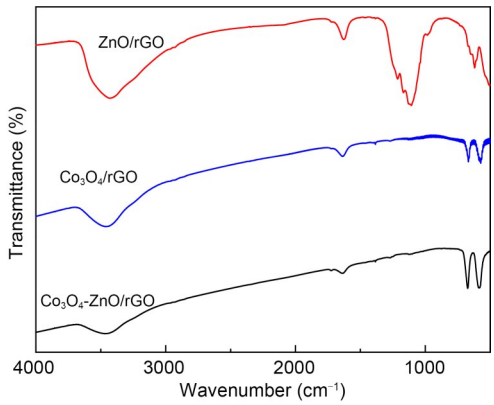

Fig. 3 FT-IR spectra of ZnO/rGO, Co_3O_4/rGO, and Co_3O_4-ZnO/rGO

3.1.3 SEM

The structure and morphology of the prepared material particles were characterized through sample SEM imaging. As shown in Fig. S1 of the electronic supplementary materials (ESM), Co_3O_4 exhibited a cubic crystal structure, aggregated and attached to a lamellar structure with folds. ZnO exhibited a hexagonal crystal structure attached to the sheet structure in the form of rods. The Co_3O_4-ZnO/rGO image in Fig. 4 shows particles of different shapes with sizes ranging from 30 to 200 nm tightly attached to the lamellar structure; some are in contact and bonded together, indicating the formation of heterojunctions.

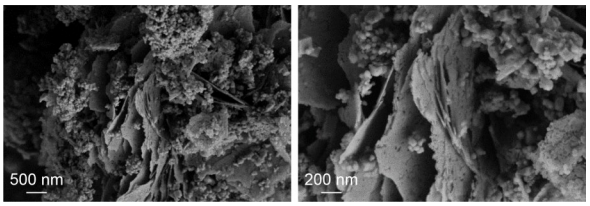

Fig. 4 SEM image of Co_3O_4-ZnO/rGO

3.1.4 XPS

XPS was used to evaluate the elemental composition of the material surface. The results are shown in Fig. 5. For Co_3O_4-ZnO/rGO, we observed peaks corresponding to C 1s, O 1s, Zn 2p, and Co 2p. In the C 1s XPS spectrum, Co_3O_4-ZnO/rGO had two distinct peaks at 284.8 and 286.5 eV, which were assigned to the C═C and C–O lattice absorption peaks in graphene, respectively (Rakibuddin and Ananthakrishnan, 2016). Two peaks are shown at O 1s for Co_3O_4-ZnO/rGO, with 530.4 and 529.9 eV corresponding to the Co_3O_4

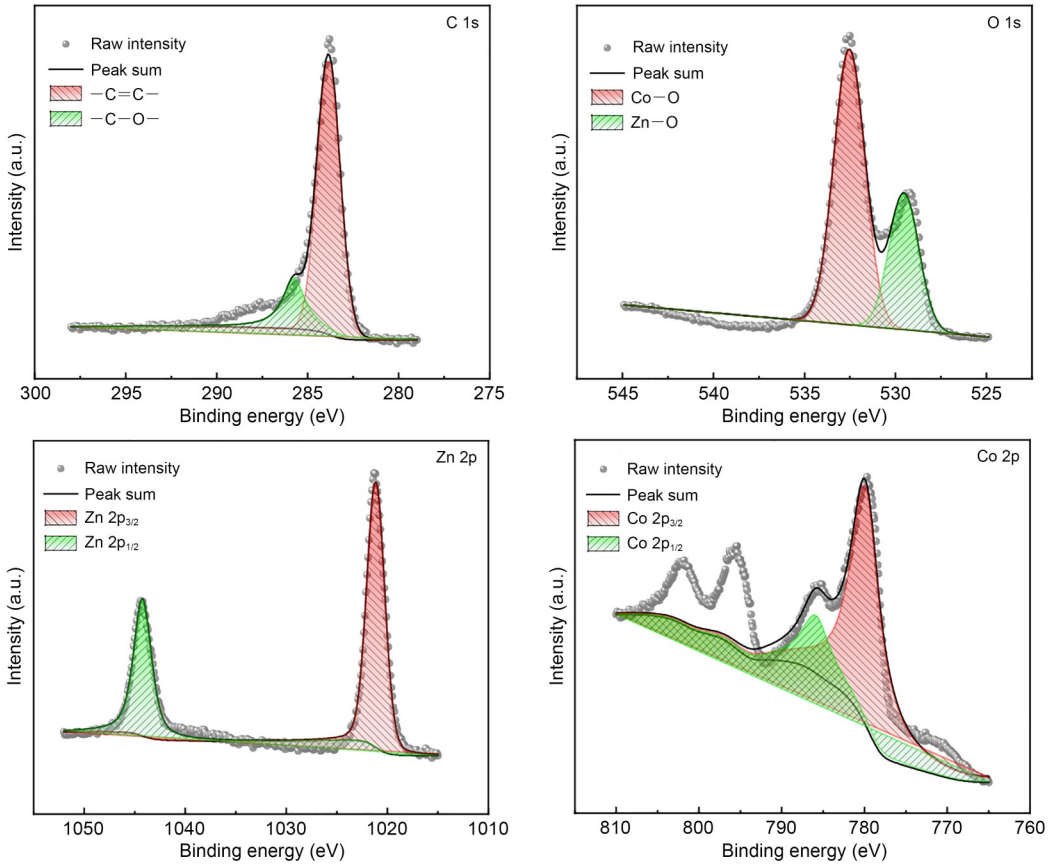

Fig. 5 XPS spectra of Co_3O_4-ZnO/rGO

and ZnO lattice oxygen peaks, respectively (Rashid et al., 2014; Zhang QS et al., 2020). Two peaks at 1021.4 ($2p_{3/2}$) and 1044.7 eV ($2p_{1/2}$) were observed for Zn 2p, whereas two peaks at 779.8 ($2p_{3/2}$) and 797.6 eV ($2p_{1/2}$) were observed for Co 2p (Rashid et al., 2014; Zhang QS et al., 2020). Fig. S2 of the ESM shows the full XPS spectra of the three materials; the results indicate that the heterojunction catalyst was composed of four elements, i.e., C, O, Co, and Zn.

3.2 Preparation and performance testing

3.2.1 Doping amount of rGO

Fig. 6 shows the relationship between rGO doping and the RhB degradation rate in Co_3O_4-ZnO/rGO. When the doping mass fraction was 0.1%–0.5%, RhB degraded more quickly as the mass percentage of rGO increased, reaching 56.24% in 40 min. We attribute this to the electrical conductivity of rGO, which increases the electron transfer efficiency of Co_3O_4-ZnO/rGO, thereby enhancing the catalytic performance. When the rGO doping mass fraction was 0.5%–0.9%, the rate of RhB degradation declined as the mass fraction of rGO doping increased. This is because too much rGO covered the active sites and reduced the catalytic performance of Co_3O_4-ZnO/rGO. The catalytic performance of Co_3O_4-ZnO/rGO was significantly better compared with that of Co_3O_4/rGO and ZnO/rGO under the same rGO doping mass fraction. In addition, the effects of rGO doping mass fraction on the degradation performance of Co_3O_4/rGO and ZnO/rGO were consistent.

3.2.2 Hydrothermal reaction time

The impact of various hydrothermal reaction periods on catalytic activity is shown in Fig. 7. The catalytic properties of Co_3O_4-ZnO/rGO changed with different hydrothermal times. The degradation rate of RhB increased as hydrothermal time increased from 2 to 4 h, and the best catalytic performance was achieved at 4 h, with an RhB degradation rate of 58.78%. At 4–6 h of hydrothermal reaction, the degradation rate of RhB slightly decreased, but exhibited little fluctuation, probably due to the continuous high-temperature and

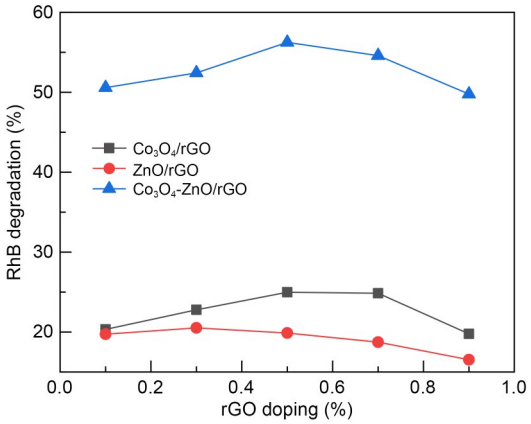

Fig. 6 Effect of rGO doping amount on RhB degradation

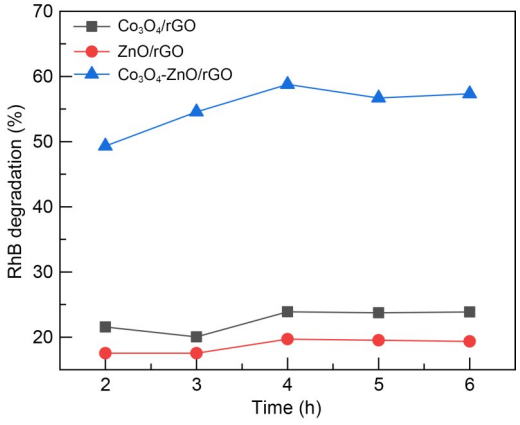

Fig. 7 Effect of hydrothermal reaction time on RhB degradation

high-pressure environment that damaged the crystal structure of Co_3O_4-ZnO/rGO, weakening the catalytic performance.

3.2.3 Calcination temperature

The catalytic performance of Co_3O_4-ZnO/rGO was affected by the temperature range, as shown in Fig. 8. When the calcination temperature was 500–700 °C, the catalytic degradation performance of Co_3O_4-ZnO/rGO was better than that at 300–500 °C, reaching 60.03% in 40 min. The catalytic performances of the products at different temperatures were different because of the different products obtained at the calcination temperatures of the intermediate product $Co(OH)_2$ that formed during hydrothermal preparation, which can degrade into Co_2O_3 at temperatures below 290 °C, into Co_3O_4 and Co_2O_3 at 290–500 °C, and into Co_3O_4 and CoO at 500–1000 °C. In addition, the small size of the corundum boat used in the calcination process,

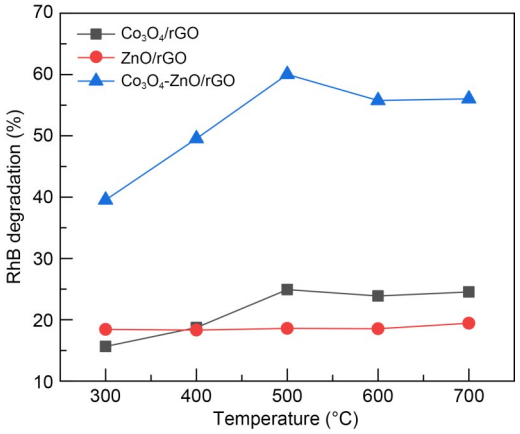

Fig. 8 Effect of calcination temperature on RhB degradation

as well as uneven internal heating, may result in the appearance of multiple products, a phenomenon that affects catalytic degradation performance. When the calcination temperature was 300–500 °C, the increase in the catalytic efficiency of Co_3O_4-ZnO/rGO with temperature was mainly caused by an increase in the yield of Co_3O_4 in the intermediate product $Co(OH)_2$ by thermal decomposition, and the purity of the prepared Co_3O_4-ZnO/rGO was improved.

3.3 Catalytic performance and stability

We investigated the RhB degradation efficiency of the UV/Co_3O_4-ZnO/rGO/PMS system. First, we tested the impact of adsorption on Co_3O_4-ZnO/rGO performance. About 7.1% of RhB was adsorbed after 40 min. Subsequently, 0.025-g PMS was added to the solution. After shaking for 40 min, the RhB degradation rate increased to approximately 27.55%. This indicates that the addition of PMS improves removal of organic matter from water. Fig. S3 of the ESM shows that the RhB degradation rate of the Co_3O_4-ZnO/rGO/PMS system was better than that of the Co_3O_4/rGO/PMS (25.43%) and ZnO/rGO/PMS (14.56%) systems under the same conditions. The pseudo-first-order reaction rate constants k of RhB degradation were 0.0051, 0.0035, and 0.0022 min^{-1}, respectively. RhB degraded at similar rates in the Co_3O_4-ZnO/rGO/PMS and Co_3O_4/rGO/PMS systems; however, both were faster than the ZnO/rGO/PMS system. This demonstrates that Co plays a key role in the reaction, because its activation effect in promoting the ability of PMS to generate $SO_4^{\bullet-}$ is significantly stronger than that of Zn.

The photocatalytic properties of three catalysts for RhB degradation were tested under visible-light

irradiation. As depicted in Fig. S4 of the ESM, in three systems, Co_3O_4/rGO/UV, ZnO/rGO/UV, and Co_3O_4-ZnO/rGO/UV, the degradation rates of RhB within 40 min were 37.65%, 21.58%, and 57.05%, respectively. RhB degradation in the Co_3O_4-ZnO/rGO/UV system had a pseudo-first-order reaction rate constant k of 0.212 min^{-1}, which was 3.36 times faster than that of the Co_3O_4/rGO/UV system (0.0063 min^{-1}) and 4.32 times faster than that of the ZnO/rGO/UV system (0.0049 min^{-1}). This suggests that photocatalytic degradation of RhB is facilitated by the generation of a Co_3O_4-ZnO heterojunction (Alshaikh et al., 2021). Moreover, the addition of PMS to the system increased RhB degradation efficiency. As shown in Fig. 9, in the UV/Co_3O_4-ZnO/rGO/PMS system, 90.40% of RhB was degraded within 40 min, indicating that the addition of PMS can produce a synergistic effect with the photocatalytic reaction and effectively promote pollutant degradation (Shao et al., 2017; Jin et al., 2020a).

Furthermore, we tested the reusability of the catalyst in the UV/Co_3O_4-ZnO/rGO/PMS system using a five-cycle test. After the fifth reaction, the degradation rate of RhB did not decrease significantly (86.30%) and was only 4.1% lower than that of the first reaction. Fig. S5 of the ESM shows the XPS spectra of the unused catalyst and the catalyst at the end of the reaction. The position and shape of each diffraction peak showed no obvious changes, demonstrating the structural stability of the Co_3O_4-ZnO/rGO. The position of Co changed slightly, while the position and intensity of other elemental peaks did not change significantly. Combined with the repeated use experiment, Co_3O_4-ZnO/rGO exhibited high stability. The decrease in degradation efficiency was caused by the loss of metal ions by the catalyst.

3.4 Mechanism

3.4.1 Involved active species

We conducted free-radical scavenging studies to identify the free radical species present during RhB degradation. The change in the RhB degradation rate over time following the addition of the inhibitor is depicted in Fig. 10. TBA and MeOH correspond to ·OH and $SO_4^{\cdot-}$, respectively, and BQ and TEOA correspond to $O_2^{\cdot-}$ and h^+, respectively. Injection of MeOH and TBA significantly slowed the process of RhB degradation in the reaction system. The effect of TBA on

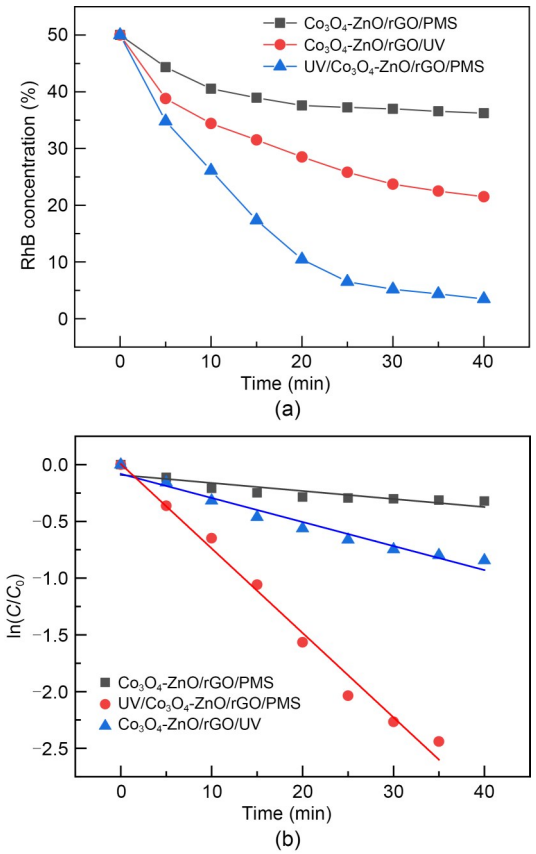

Fig. 9 Degradation of RhB in different systems: (a) RhB treatment efficiency; (b) pseudo-first-order kinetic plot. C is the RhB concentration at time t, and C_0 is the initial concentration of RhB

the RhB degradation rate was the greatest, causing it to decrease from 91.28% to 57.05%, whereas the rate constant decreased from 0.0773 to 0.0249 min^{-1}, indicating that ·OH was the main reactive group in the reaction process. The addition of MeOH reduced the degradation rate of RhB by 24.55%, indicating that $SO_4^{\cdot-}$ was the main oxidizing species during the reaction. However, RhB degradation was not significantly affected by the addition of BQ and TEOA to the reaction system, demonstrating that few $O_2^{\cdot-}$ or h^+ were generated in the system to participate in the reaction.

3.4.2 Band gap width and photoresponse range

UV-Vis diffuse reflectance spectroscopy was used to evaluate the light-trapping performance of Co_3O_4-ZnO/rGO, and the results are shown in Fig. 11a. The band gap edges of Co_3O_4-ZnO/rGO were all approximately 732 nm. We observed two distinctive characteristic peaks at 590 and 610 nm, which were consistent

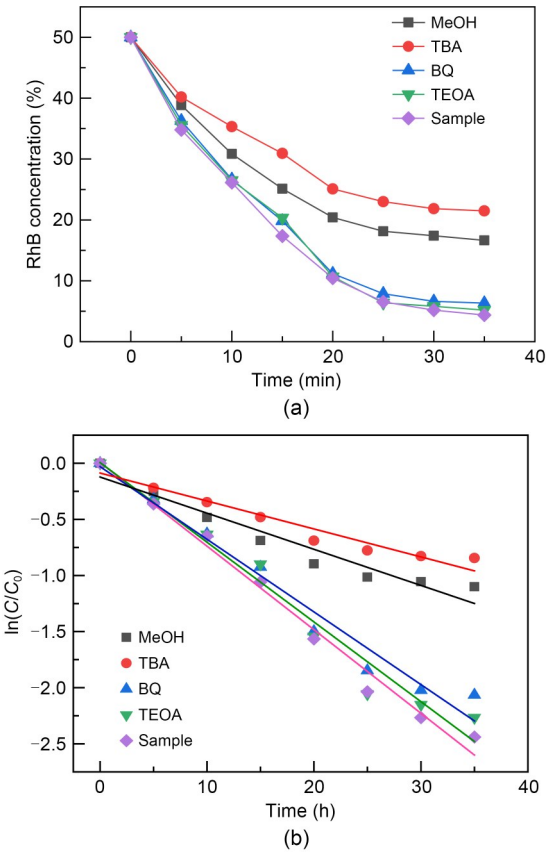

Fig. 10 Effects of active species on RhB degradation: (a) RhB treatment efficiency; (b) pseudo-first-order kinetic plot

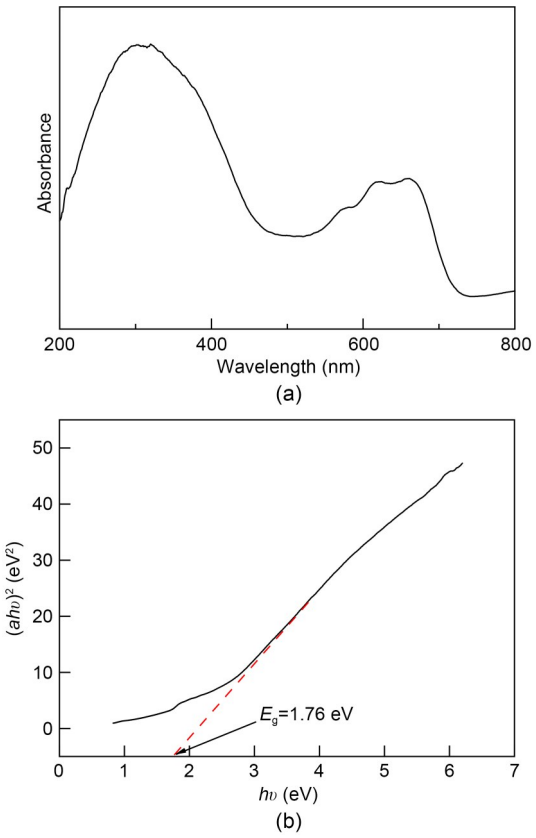

Fig. 11 UV-Vis DRS spectra (a) and $(ahv)^2$ and hv plots (b) of the samples

with the jump in the tetrahedral coordination structure of the Co (II) ion. Comparing our findings with those of Su et al. (2022), the peak position was slightly red-shifted, which may be because the ZnO in Co_3O_4-ZnO/rGO entered the lattice of Co_3O_4. The relationship between the $(ahv)^2$ and hv curves is illustrated in Fig. 11b, where a, h, and v represent the absorption coefficient, Planck's constant, and incident light frequency, respectively. According to Eq. (1), where χ is the electronegativity of the semiconductor (about 5.0 eV) and E_e is the free electron energy on the hydrogen scale (4.3 eV), the Co_3O_4-ZnO/rGO valence band (E_{VB}) can be estimated to be 1.58 eV (Wang et al., 2019). In addition, according to Eq. (2), the conduction band (E_{CB}) of Co_3O_4-ZnO/rGO is −0.18 eV, where E_g is the band gap of the semiconductor energy (1.76 eV) (Zou et al., 2018).

$$E_{VB}=\chi-E_e+\frac{E_g}{2}, \quad (1)$$

$$E_{CB}=E_{VB}-E_g. \quad (2)$$

3.4.3 Bonding process and Co valence change

Anipsitakis et al. (2005) proved that Co_3O_4 activated PMS to produce $SO_4^{\cdot-}$. Fig. 12 shows the FT-IR spectrum of the interaction between Co_3O_4-ZnO/rGO and PMS. The stretching vibration peaks of SO_4^{2-} and HSO_5^- were located at 1103 and 1249 cm^{-1}, respectively. The Co_3O_4-ZnO/rGO surface hydroxyl peak was located at 3243 cm^{-1}, the Zn–O peak at 483 cm^{-1}, and the Co–O peak at 572 cm^{-1}.

When Co_3O_4-ZnO/rGO was added to the PMS aqueous solution, the intensity of the peak at 1103 cm^{-1} was substantially higher compared to that of the peak at 1149 cm^{-1}. This indicates that PMS began to decompose, producing SO_4^{2-}. The peaks at 1249 and 1103 cm^{-1} showed blue shifts of 8 and 4 cm, respectively, indicating that the S–O bond was strengthened after Co_3O_4-ZnO/rGO was bonded to the surface of PMS. It is possible that the –OH in S–O–(OH) weakens the attraction to the electron cloud generated by the S–O bond, resulting in the Co (II) of Co_3O_4-ZnO/rGO donating electrons to the –OH groups in PMS.

After we added PMS to the Co_3O_4-ZnO/rGO aqueous solution, the surface hydroxyl peak (3243 cm^{-1}) showed a red shift of 20 cm. This indicates that HSO_5^- replaced part of the surface hydroxyl peaks to bond with the surface metal elements of Co_3O_4-ZnO/rGO during the reaction. Simultaneously, the electron-withdrawing effect of Co (III) may have led to its bonding to the hydroxyl group.

Fig. S6 of the ESM shows the XPS patterns of the changes in Co (II) and Co (III) contents in the system before and after the reaction. The molar ratios of Co (II) and Co (III) before the reaction were 35.13% and 64.87%, respectively, whereas those after the reaction were 13.86% and 86.14%, indicating the conversion of Co (II) to Co (III) during the entire reaction process.

The reaction process involves the transfer of electrons through the conversion of different valence states of Co, and the photogenerated carriers can increase the rate of change in the Co valence states. Co_3O_4-ZnO/rGO itself acts as a catalyst to accelerate the reaction process, but its properties do not change. This shows that in the synergistic oxidation reaction system, Co participates in production of $SO_4^{\cdot-}$, which leads to the conversion of Co (II) to Co (III). Therefore, it can be inferred that photocatalysis increases the yield of $SO_4^{\cdot-}$ in the Co_3O_4-ZnO/rGO/PMS reaction system, and that the Co (II) or Co (III) created during the $SO_4^{\cdot-}$ production process further reduces the recombination efficiency of electron-hole pairs.

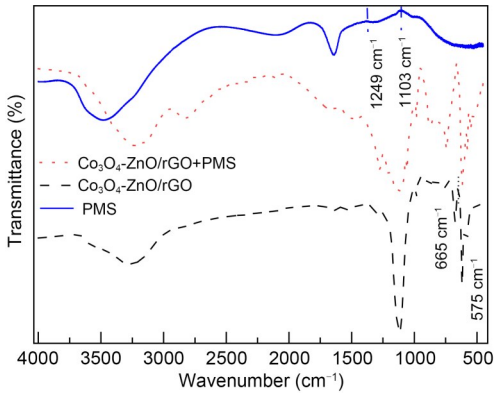

Fig. 12 FT-IR spectra of the interaction between Co_3O_4-ZnO/rGO and PMS

3.4.4 Potential mechanism

Based on the results discussed above, we proposed a mechanism for RhB degradation in the UV/Co_3O_4-ZnO/rGO/PMS system. First, rGO has a large specific surface area, which offers additional active sites for subsequent reactions, and its electrical conductivity enhances electron-transfer efficiency in the reaction system (Xu et al., 2021). Second, the increased light-harvesting capacity permits Co_3O_4-ZnO/rGO to acquire more photon energy, and heterojunction formation between Co_3O_4 and ZnO reduces the rate at which electron-hole pairs recombine and improves the catalytic ability of the catalyst, which can be also proved from the photoluminescence fluorescence spectrum. Compared with Co_3O_4/rGO and ZnO/rGO, the fluorescence intensity of Co_3O_4-ZnO/rGO is significantly reduced, indicating that the recombination rate of photogenerated electron-hole pairs is reduced and the separation efficiency of photogenerated electrons and holes is improved (Rakibuddin and Ananthakrishnan, 2016; Zhang QS et al., 2020).

As shown in Fig. 13, when Co_3O_4-ZnO/rGO was exposed to visible light, the electrons in the valence band (VB) of both Co_3O_4 and ZnO could be stimulated and transported to their respective conduction band (CB). In addition, under the interference of the built-in electric field, the electrons in the CB of Co_3O_4 were gradually transported to the CB of ZnO, triggering PMS to produce $SO_4^{\cdot-}$. Similarly, the holes produced by the VB in ZnO were transported to the VB in Co_3O_4, where they interacted with PMS to generate $SO_5^{\cdot-}$, which in turn generated $SO_4^{\cdot-}$ (Jin et al., 2020b; Velmurugan et al., 2021). $SO_4^{\cdot-}$ can also react with water to form ·OH. This effectively reduces the binding of electron-hole pairs and induces more electrons to participate in the degradation process, thereby increasing the reaction rate. Moreover, Co_3O_4 exhibited excellent PMS activation performance, generating more $SO_4^{\cdot-}$ in the solution under the action of Co (II). Importantly, the free electrons in the solution also accelerated the cycle of Co (II) and Co (III). Finally, the UV/Co_3O_4-ZnO/rGO/PMS system degraded RhB into CO_2 and H_2O under the action of the main active substances $SO_4^{\cdot-}$ and ·OH.

5 Conclusions

(1) Co_3O_4-ZnO/rGO heterojunction catalysts were synthesized using a hydrothermal method. The distinct particle/sheet structure of Co_3O_4-ZnO/rGO offers a large surface area with numerous active sites for the

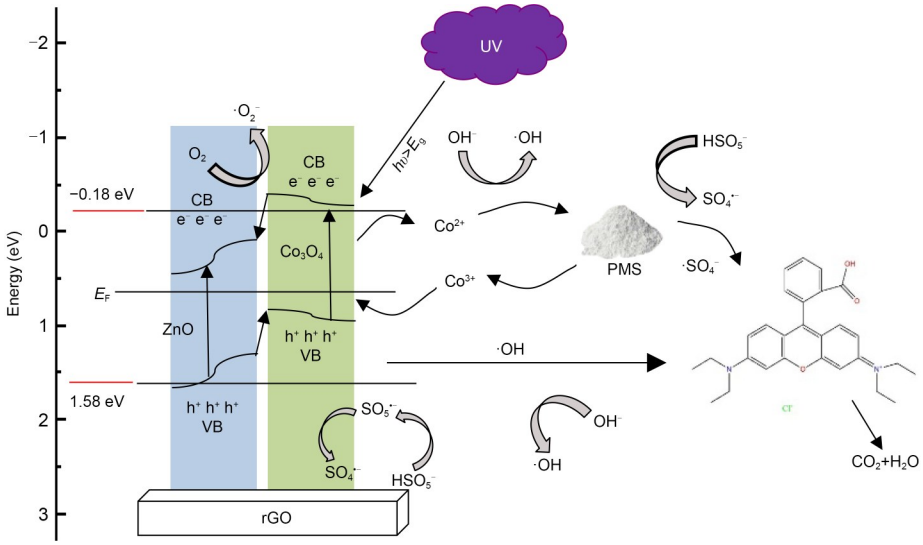

Fig. 13 Potential mechanism of RhB degradation in the UV/Co_3O_4-ZnO/rGO/PMS system (E_F: Fermi level)

reaction, which enables the extension of the carrier lifetime and speeds up the transport and separation of electron-hole pairs, resulting in superior photocatalytic efficiency and the ability to activate PMS compared to stand-alone Co_3O_4 or ZnO.

(2) PMS and photocatalysis exhibit good synergy. PMS better suppresses electron-hole pair recombination by capturing electrons, and the photogenerated carriers generated by illumination also strengthen the redox cycle between Co (II) and Co (III), resulting in more active radicals.

(3) Co_3O_4-ZnO/rGO exhibited a good ability to trigger PMS for RhB degradation in the SR-photo system. In the presence of major radicals, such as $SO_4^{\cdot-}$ and ·OH, the UV/Co_3O_4-ZnO/rGO/PMS system cleared 90.4% of the RhB in 40 min.

(4) This study may offer a viable solution for water pollution remediation as well as a reference for designing more effective heterojunction catalysts based on a combination of PMS and photocatalytic technology. Further work is needed to investigate the performance of Co_3O_4-ZnO/rGO materials for visual-light-driven catalytic degradation of organic pollutants in natural water bodies.

Acknowledgments

This work is supported by the National Natural Science Foundation of China (No. 21906012).

Author contributions

Zhanmei ZHANG designed the research and revised and edited the final version. Xilin CHEN and Ziran HUANG processed the corresponding data. Yi ZHANG wrote the first draft of the manuscript. Zuqin ZOU and Huaili ZHENG helped to organize the manuscript.

Conflict of interest

Zhanmei ZHANG, Yi ZHANG, Xilin CHEN, Ziran HUANG, Zuqin ZOU, and Huaili ZHENG declare that they have no competing financial interests or personal relationships that could have appeared to influence the work reported in this paper.

References

Akbarzadeh E, Soheili HZ, Hosseinifard M, et al., 2020. Preparation and characterization of novel Ag_3VO_4/Cu-MOF/rGO heterojunction for photocatalytic degradation of organic pollutants. *Materials Research Bulletin*, 121: 110621. https://doi.org/10.1016/j.materresbull.2019.110621

Alshaikh H, Shawky A, Mohamed RM, et al., 2021. Solution-based synthesis of Co_3O_4/ZnO p-n heterojunctions for rapid visible-light-driven oxidation of ciprofloxacin. *Journal of Molecular Liquids*, 334:116092. https://doi.org/10.1016/j.molliq.2021.116092

Anipsitakis GP, Stathatos E, Dionysiou DD, 2005. Heterogeneous activation of Oxone using Co_3O_4. *The Journal of Physical Chemistry B*, 109(27):13052-13055. https://doi.org/10.1021/jp052166y

Cao J, Yang ZH, Xiong WP, et al., 2020. Peroxymonosulfate activation of magnetic Co nanoparticles relative to an N-doped porous carbon under confinement: boosting stability and performance. *Separation and Purification Technology*, 250:117237. https://doi.org/10.1016/j.seppur.2020.117237

Dong CJ, Xiao XC, Chen G, et al., 2015. Synthesis and photocatalytic degradation of methylene blue over p-n junction Co_3O_4/ZnO core/shell nanorods. *Materials Chemistry and*

Physics, 155:1-8.
https://doi.org/10.1016/j.matchemphys.2015.01.033

El-Molla SA, Ali LI, Mahmoud HR, et al., 2017. Effect of preparation method, loading of Co_3O_4 and calcination temperature on the physicochemical and catalytic properties of Co_3O_4/ZnO nanomaterials. *Materials Chemistry and Physics*, 185:44-54.
https://doi.org/10.1016/j.matchemphys.2016.10.003

Gautam S, Agrawal H, Thakur M, et al., 2020. Metal oxides and metal organic frameworks for the photocatalytic degradation: a review. *Journal of Environmental Chemical Engineering*, 8(3):103726.
https://doi.org/10.1016/j.jece.2020.103726

Ghanbari F, Moradi M, 2017. Application of peroxymonosulfate and its activation methods for degradation of environmental organic pollutants: review. *Chemical Engineering Journal*, 310:41-62.
https://doi.org/10.1016/j.cej.2016.10.064

Guo H, Niu HY, Liang C, et al., 2020. Few-layer graphitic carbon nitride nanosheet with controllable functionalization as an effective metal-free activator for peroxymonosulfate photocatalytic activation: role of the energy band bending. *Chemical Engineering Journal*, 401:126072.
https://doi.org/10.1016/j.cej.2020.126072

Guo J, Shen CH, Sun J, et al., 2021. Highly efficient activation of peroxymonosulfate by Co_3O_4/Bi_2MoO_6 p-n heterostructure composites for the degradation of norfloxacin under visible light irradiation. *Separation and Purification Technology*, 259:118109.
https://doi.org/10.1016/j.seppur.2020.118109

Guo Y, Dai YX, Zhao W, et al., 2018. Highly efficient photocatalytic degradation of naphthalene by Co_3O_4/$Bi_2O_2CO_3$ under visible light: a novel p–n heterojunction nanocomposite with nanocrystals/lotus-leaf-like nanosheets structure. *Applied Catalysis B: Environmental*, 237:273-287.
https://doi.org/10.1016/j.apcatb.2018.05.089

Han CC, Ge L, Chen CF, et al., 2014. Novel visible light induced Co_3O_4-g-C_3N_4 heterojunction photocatalysts for efficient degradation of methyl orange. *Applied Catalysis B: Environmental*, 147:546-553.
https://doi.org/10.1016/j.apcatb.2013.09.038

Han WY, Li DG, Zhang MQ, et al., 2020. Photocatalytic activation of peroxymonosulfate by surface-tailored carbon quantum dots. *Journal of Hazardous Materials*, 395:122695.
https://doi.org/10.1016/j.jhazmat.2020.122695

Jin CY, Kang J, Li ZL, et al., 2020a. Enhanced visible light photocatalytic degradation of tetracycline by MoS_2/Ag/g-C_3N_4 Z-scheme composites with peroxymonosulfate. *Applied Surface Science*, 514:146076.
https://doi.org/10.1016/j.apsusc.2020.146076

Jin CY, Wang M, Li Z, et al., 2020b. Two dimensional Co_3O_4/g-C_3N_4 Z-scheme heterojunction: mechanism insight into enhanced peroxymonosulfate-mediated visible light photocatalytic performance. *Chemical Engineering Journal*, 398:125569.
https://doi.org/10.1016/j.cej.2020.125569

Li F, Dong B, 2019. Facile two-step synthesis of Ag nanoparticles dispersed on N, S co-doped RGO for highly efficient plasmonic photocatalytic water purification. *Catalysis Communications*, 119:42-45.
https://doi.org/10.1016/j.catcom.2018.10.013

Lou YB, Zhang YK, Cheng L, et al., 2018. A stable plasmonic Cu@Cu_2O/ZnO heterojunction for enhanced photocatalytic hydrogen generation. *ChemSusChem*, 11(9):1505-1511.
https://doi.org/10.1002/cssc.201800249

Malefane ME, Feleni U, Kuvarega AT, 2020. Cobalt (II/III) oxide and tungsten (VI) oxide p-n heterojunction photocatalyst for photodegradation of diclofenac sodium under visible light. *Journal of Environmental Chemical Engineering*, 8:103560.
https://doi.org/10.1016/j.jece.2019.103560

Rakibuddin M, Ananthakrishnan R, 2016. Effective photocatalytic dechlorination of 2, 4-dichlorophenol by a novel graphene encapsulated ZnO/Co_3O_4 core–shell hybrid under visible light. *Photochemical & Photobiological Sciences*, 15(1):86-98.
https://doi.org/10.1039/C5PP00305A

Rashid J, Barakat MA, Mohamed RM, et al., 2014. Enhancement of photocatalytic activity of zinc/cobalt spinel oxides by doping with ZrO_2 for visible light photocatalytic degradation of 2-chlorophenol in wastewater. *Journal of Photochemistry and Photobiology A: Chemistry*, 284:1-7.
https://doi.org/10.1016/j.jphotochem.2014.03.017

Reda GM, Fan HQ, Tian HL, 2017. Room-temperature solid state synthesis of Co_3O_4/ZnO p–n heterostructure and its photocatalytic activity. *Advanced Powder Technology*, 28(3):953-963.
https://doi.org/10.1016/j.apt.2016.12.025

Ren JT, Zheng YL, Yuan K, et al., 2020. Self-templated synthesis of Co_3O_4 hierarchical nanosheets from a metal–organic framework for efficient visible-light photocatalytic CO_2 reduction. *Nanoscale*, 12(2):755-762.
https://doi.org/10.1039/c9nr08669b

Ren WJ, Gao JK, Lei C, et al., 2018. Recyclable metal-organic framework/cellulose aerogels for activating peroxymonosulfate to degrade organic pollutants. *Chemical Engineering Journal*, 349:766-774.
https://doi.org/10.1016/j.cej.2018.05.143

Shao H, Zhao X, Wang Y, et al., 2017. Synergetic activation of peroxymonosulfate by Co_3O_4 modified g-C_3N_4 for enhanced degradation of diclofenac sodium under visible light irradiation. *Applied Catalysis B: Environmental*, 218:810-818.
https://doi.org/10.1016/j.apcatb.2017.07.016

Shen CH, Wen XJ, Fei ZH, et al., 2020. Visible-light-driven activation of peroxymonosulfate for accelerating ciprofloxacin degradation using CeO_2/Co_3O_4 p-n heterojunction photocatalysts. *Chemical Engineering Journal*, 391:123612.
https://doi.org/10.1016/j.cej.2019.123612

Su P, Zhang XJ, Hao XQ, et al., 2022. Co_3O_4 modified $Mn_{0.2}Cd_{0.8}S$ with different shells forms p-n heterojunction to optimize energy/mass transfer for efficient photocatalytic hydrogen evolution. *Separation and Purification Technology*, 285:120318.

https://doi.org/10.1016/j.seppur.2021.120318

Tang CN, Liu EZ, Wan J, et al., 2016. Co_3O_4 nanoparticles decorated Ag_3PO_4 tetrapods as an efficient visible-light-driven heterojunction photocatalyst. *Applied Catalysis B: Environmental*, 181:707-715. https://doi.org/10.1016/j.apcatb.2015.08.045

Thakur K, Kandasubramanian B, 2019. Graphene and graphene oxide-based composites for removal of organic pollutants: a review. *Journal of Chemical & Engineering Data*, 64(3):833-867. https://doi.org/10.1021/acs.jced.8b01057

Velmurugan S, Yang TCK, Chen SW, et al., 2021. Metal-organic frameworks derived ZnO-Co_3O_4 pn heterojunction photocatalyst for the photoelectrochemical detection of sulfadiazine. *Journal of Environmental Chemical Engineering*, 9(5):106169. https://doi.org/10.1016/j.jece.2021.106169

Wang M, Zhang Y, Jin CY, et al., 2019. Fabrication of novel ternary heterojunctions of Pd/g-C_3N_4/Bi_2MoO_6 hollow microspheres for enhanced visible-light photocatalytic performance toward organic pollutant degradation. *Separation and Purification Technology*, 211:1-9. https://doi.org/10.1016/j.seppur.2018.09.061

Xu P, Wang P, Wang Q, et al., 2021. Facile synthesis of Ag_2O/ZnO/rGO heterojunction with enhanced photocatalytic activity under simulated solar light: kinetics and mechanism. *Journal of Hazardous Materials*, 403:124011. https://doi.org/10.1016/j.jhazmat.2020.124011

Yang J, Wang MY, Zhao SS, et al., 2019. Petal-biotemplated synthesis of two-dimensional Co_3O_4 nanosheets as photocatalyst with enhanced photocatalytic activity. *International Journal of Hydrogen Energy*, 44(2):870-879. https://doi.org/10.1016/j.ijhydene.2018.11.027

Yang ZH, Cao J, Chen YP, et al., 2019. Mn-doped zirconium metal-organic framework as an effective adsorbent for removal of tetracycline and Cr(VI) from aqueous solution. *Microporous and Mesoporous Materials*, 277:277-285. https://doi.org/10.1016/j.micromeso.2018.11.014

Zhang JL, Zhai CY, Zhao W, et al., 2020. Insight into combining visible-light photocatalysis with transformation of dual metal ions for enhancing peroxymonosulfate activation over dibismuth copper oxide. *Chemical Engineering Journal*, 397:125310. https://doi.org/10.1016/j.cej.2020.125310

Zhang JL, Zhao W, Li Z, et al., 2021. Visible-light-assisted peroxymonosulfate activation over Fe(II)/V(IV) self-doped $FeVO_4$ nanobelts with enhanced sulfamethoxazole degradation: performance and mechanism. *Chemical Engineering Journal*, 403:126384. https://doi.org/10.1016/j.cej.2020.126384

Zhang QS, Xiao Y, Li YM, et al., 2020. Efficient photocatalytic overall water splitting by synergistically enhancing bulk charge separation and surface reaction kinetics in Co_3O_4–decorated ZnO@ZnS core-shell structures. *Chemical Engineering Journal*, 393:124681. https://doi.org/10.1016/j.cej.2020.124681

Zou WX, Deng B, Hu XX, et al., 2018. Crystal-plane-dependent metal oxide-support interaction in CeO_2/g-C_3N_4 for photocatalytic hydrogen evolution. *Applied Catalysis B: Environmental*, 238:111-118. https://doi.org/10.1016/j.apcatb.2018.07.022

Electronic supplementary materials

Figs. S1–S6